
Article:
Bones, DL orcid.org/0000-0003-1394-023X, Daly, SM orcid.org/0000-0001-7957-4514, Mangan, TP orcid.org/0000-0001-7053-5594 et al. (1 more author) (2020) A study of the reactions of Ni^+ and NiO^+ ions relevant to planetary upper atmospheres. Physical Chemistry Chemical Physics, 22 (16). pp. 8940-8951. ISSN 1463-9076

https://doi.org/10.1039/D0CP01124J

CP-ART-02-2020-001124

A Study of the reactions of Ni^+ and NiO^+ ions relevant to planetary upper atmospheres

David L. Bones, Shane M. Daly, Thomas P. Mangan and John M. C. Plane*

School of Chemistry, University of Leeds, Leeds, United Kingdom

* Corresponding author. Email: j.m.c.plane@leeds.ac.uk

Submitted to *Physical Chemistry Chemical Physics*

February 2020

Revised April 2020

Abstract

The reactions between $Ni^+(^2D)$ and O_3, O_2, N_2, CO_2 and H_2O were studied at 294 K using the pulsed laser ablation at 532 nm of a nickel metal target in a fast flow tube, with mass spectrometric detection of Ni^+ and NiO^+. The rate coefficient for the reaction of Ni^+ with O_3 is k(294 K) = (9.7 ± 2.1) × 10^{-10} cm^3 $molecule^{-1}$ s^{-1}; the reaction proceeds at the ion-permanent dipole enhanced Langevin capture rate with a predicted $T^{-0.16}$ dependence. Electronic structure theory calculations were combined with Rice-Ramsperger-Kassel-Markus theory to extrapolate the measured recombination rate coefficients to the temperature and pressure conditions of planetary upper atmospheres. The following low-pressure limiting rate coefficients were obtained for T = 120 – 400 K and He bath gas (in cm^6 $molecule^{-2}$ s^{-1}, uncertainty ±σ at 180 K): $\log_{10}(k, Ni^+ + N_2)$ = -27.5009 + 1.0667$\log_{10}(T)$ - 0.74741$(\log_{10}(T))^2$, σ=29%; $\log_{10}(k, Ni^+ + O_2)$ = -27.8098 + 1.3065$\log_{10}(T)$ - 0.81136$(\log_{10}(T))^2$, σ=32%; $\log_{10}(k, Ni^+ + CO_2)$ = -29.805 + 4.2282$\log_{10}(T)$ - 1.4303$(\log_{10}(T))^2$, σ=28%; $\log_{10}(k, Ni^+ + H_2O)$ = -24.318 + 0.20448$\log_{10}(T)$ - 0.66676$(\log_{10}(T))^2$, σ=28%). Other rate coefficients measured (at 294 K, in cm^3 $molecule^{-1}$ s^{-1}) were: k(NiO^+ + O) = (1.7 ± 1.2) × 10^{-10}; k(NiO^+ + CO) = (7.4 ± 1.3) × 10^{-11}; k(NiO^+ + O_3) = (2.7 ± 1.0) × 10^{-10} with (29 ± 21)% forming Ni^+ as opposed to NiO_2^+; k(NiO_2^+ + O_3) = (2.9 ± 1.4) × 10^{-10}, with (16 ± 9)% forming NiO^+ as opposed to $ONiO_2^+$; and k($Ni^+.N_2$ + O) = (7 ± 4) × 10^{-12}. The chemistry of Ni^+ and NiO^+ in the upper atmospheres of Earth and Mars is then discussed.

1. Introduction

The ablation of cosmic dust particles injects a variety of metals including Ni and Fe into planetary upper atmospheres.[1] A recent estimate of the dust flux from comets and asteroids into the terrestrial atmosphere is 28 ± 12 tonnes per day.[2] About 0.3 tonnes of this is Ni (based on carbonaceous chondritic abundances), of which 39% ablates in the mesosphere-lower thermosphere (MLT) region between 75 and 110 km where the μm-sized dust particles heat up and melt during atmospheric entry.[2]

The injection of these metals gives rise to layers of metal atoms and ions in the MLT.[1] Most work has focused on the Na and Fe layers, because these metals can be observed relatively easily from the ground using resonance lidars.[3] The Fe layer peaks at around 85 km in altitude, with a density up to around 20,000 atom cm^{-3}.[4] In 2015, the mesospheric Ni layer was observed for the first time by resonance lidar at Fairbanks, Alaska [5]. The layer was reported to have a peak density of ~16,000 atom cm^{-3} at a height of 87 km, which is within a factor of 2 of the Fe layer peak at the same location and season. This was unexpected because the relative Ni to Fe ratio in carbonaceous chondrites is 1:18.[6] Indeed, a more recent set of lidar measurements at Kühlungsborn, Germany, found the Ni peak density varied between 280 and 450 atom cm^{-3}, which is only a factor of ~2 lower than the chondritic ratio.[7] A notable feature in both lidar studies is that the vertical profile of the Ni layer is broader than the Fe layer, suggesting that somewhat different gas-phase chemistry may be occurring. Metallic ions in the MLT have mostly been observed by rocket-borne mass spectrometry.[8] As

shown in our recent study on cosmic dust sources,[2] the Ni^+:Fe^+ ratio in the MLT is very close to the chondritic ratio (see Figure 7 in that paper). Ni^+ has also been observed recently in the upper atmosphere of Mars (120 – 180 km) by a mass spectrometer on the MAVEN spacecraft; the Ni^+:Fe^+ ratio is within a factor of 2 of the chondritic ratio.[2]

The present study is motivated by the need to understand the ion-molecule chemistry that partitions nickel between Ni and Ni^+ above 90 km in the terrestrial atmosphere (we have recently published a laboratory study of the reaction kinetics of neutral nickel species[9]). Figure 1 is a schematic of the likely chemistry in the terrestrial atmosphere, based on the chemistry of other meteoric metals such as Fe, Mg and Ca.[3] Ni^+ ions will be produced in the MLT through charge transfer of Ni atoms with ambient NO^+ and O_2^+ ions, photo-ionization, and also directly during atmospheric entry when the freshly ablated Ni can ionize through hyperthermal collisions with air molecules.[3] NiO^+ can also form directly through the reaction of Ni with ambient O_2^+ ions.[10]

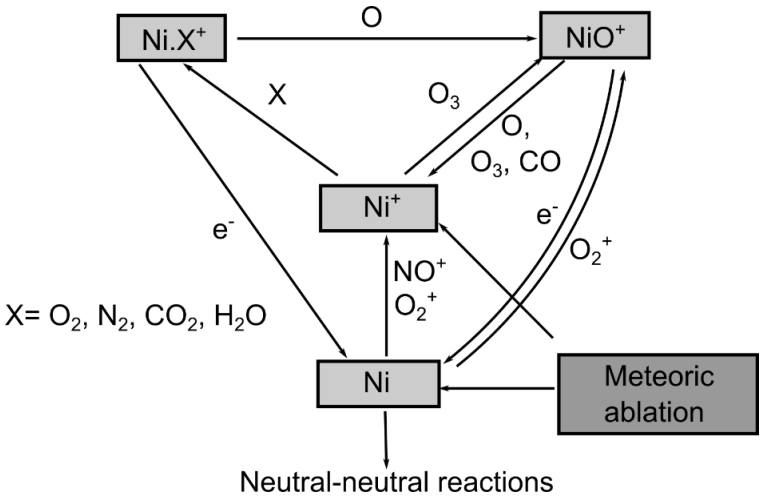

Figure 1. Reaction scheme for the ion-molecule chemistry of Ni^+ in the Earth's mesosphere and lower thermosphere.

The oxidation of Ni^+ to NiO^+ is then likely to proceed via reaction with O_3:

$Ni^+ + O_3 \rightarrow NiO^+ + O_2$ $\quad \Delta H^\ominus = -125$ [-157 ± 19] kJ mol^{-1} (R1)

NiO^+ can react further with O_3 to produce higher oxides, or be recycled to Ni^+ by reaction with O_3, CO or O:

$NiO^+ + O_3 \rightarrow Ni^+ + 2O_2$ $\quad \Delta H^\ominus = -184$ [-136 ± 19] kJ mol^{-1} (R2a)

$\rightarrow NiO_2^+ + O_2$ $\quad \Delta H^\ominus = -259$ kJ mol^{-1} (R2b)

$NiO_2^+ + O_3 \rightarrow NiO^+ + 2O_2$ $\quad \Delta H^\ominus = -61$ kJ mol^{-1} (R3a)

$\rightarrow ONiO_2^+ + O_2$ $\quad \Delta H^\ominus = -142$ kJ mol^{-1} (R3b)

$NiO^+ + O \rightarrow Ni^+ + O_2$ $\quad \Delta H^\ominus = -284$ [-237 ± 19] kJ mol^{-1} (R4)

$NiO^+ + CO \rightarrow Ni^+ + CO_2$ $\quad \Delta H^\ominus = -195$ [-269 ± 19] kJ mol^{-1} (R5)

where the reaction enthalpies (at 0 K) are calculated at the B3LYP/aug-cc-pVQZ level of theory (see Section 4), and those shown in parentheses use the experimental bond energies $D_0(Ni^+\text{-}OH) = 235 \pm 19$ kJ mol^{-1} [11] and $D_0(Ni^+\text{-}O) = 257 \pm 19$ kJ mol^{-1}.[12] Note that the ground electronic state of NiO^+ is $^4\Sigma^-$, so in the case of R5 we assume that spin is conserved and the Ni^+ forms in the low-lying $Ni^+(^4F)$ state, which is 8394 cm^{-1} above the $Ni^+(^2D)$ ground state.[13]

Ni^+ can also potentially undergo recombination reactions with a number of molecules relevant to planetary upper atmospheres:

$Ni^+ + N_2 (+ M) \rightarrow Ni^+.N_2$ $\quad \Delta H^\ominus = -112$ kJ mol^{-1} (R6)

$Ni^+ + O_2 (+ M) \rightarrow NiO_2^+$ $\quad \Delta H^\ominus = -74$ kJ mol^{-1} (R7)

$Ni^+ + CO_2 (+ M) \rightarrow Ni^+.CO_2$ $\quad \Delta H^\ominus = -109$ kJ mol^{-1} (R8)

$Ni^+ + H_2O (+ M) \rightarrow Ni^+.H_2O$ $\quad \Delta H^\ominus = -168$ kJ mol^{-1} (R9)

where M is a third body, and the dot notation is used to indicate a cluster ion where the bond with the Ni^+ is primarily electrostatic in nature (e.g. ion-induced dipole), rather than chemical. All of these molecular ions can then undergo dissociative recombination with electrons, which will typically produce Ni atoms. Note that radiative (or dielectronic) recombination of Ni^+ with electrons should - by analogy with Fe^+ ions[3, 14] - only be significant in the thermosphere above 120 km where the atmospheric pressure is very low, and so is not included in Figure 1.

Here we report an experimental study of the kinetics of reactions R1 – 9, complemented where appropriate with theory in order to extrapolate to temperature and pressure regimes of atmospheric interest. Lastly, the relative importance of these reactions in the upper atmospheres of Earth and Mars is examined.

2. Experimental

The Laser Ablation - Fast flow tube - Mass Spectrometer (LA-FT-MS) system used to study reactions R1 – R9 was very similar to that used to study reactions of Al^+,[15] Fe^+,[16] Ca^+ [17] and Mg^+ ions,[18] and so only a brief description is given here. The stainless steel flow tube, with an internal diameter of 35.0 mm, consists of cross-pieces and nipple sections connected by conflat flanges and sealed with Viton or copper gaskets. A Nd:YAG laser (Continuum Surelite, pulse energy = ~25 mJ at 532 nm) was used to generate pulses of Ni^+ ions by ablating a Ni rod in the upstream section of the flow tube. The ions were then entrained in a He carrier gas flow 2.6–3.3 slm and transported down the tube to the skimmer cone of a quadrupole mass spectrometer (Hiden HPR60), 973 mm from the Ni rod. This skimmer cone had a 0.4 mm orifice and was biased at -17 V. As in our previous study,[15] there was no evidence of weakly-bound clusters dissociating during acceleration through the cone. Downstream of the rod, the reagent gas was added via a sliding injector, allowing several milliseconds for reaction before the skimmer cone. An Edwards E2M80 pump with a roots blower (Edwards EH500A) maintained a constant pressure in the flow tube of 1-4 Torr. Flow

velocities in the tube were typically 70 m s^{-1}, resulting in reaction times of 8 - 40 ms. All the experiments reported here were conducted at 294 K.

O_3 was generated by flowing O_2 through a high voltage corona in a commercial ozonizer, and its concentration measured by optical absorption at 253.7 nm in a 19 cm pathlength optical cell downstream of the ozoniser. This resulted in O_3 concentrations ranging from 1.5 to 4% of the O_2 concentration, depending on the ozoniser voltage and the O_2 flow rate. Atomic O was generated by flowing N_2 through a microwave discharge (McCarroll cavity, Opthos Instruments Inc.), and titrating the resulting N atoms with NO.[19] The O atoms were introduced by sliding injector, downstream of the Ni rod. The concentration of O at the point of injection was measured via titration with NO_2 added upstream of the injector. This was achieved by operating the mass spectrometer in neutral mode and determining the fraction of NO_2 removed when the O atoms were injected. The first-order loss rate of O to the walls of the flow tube was determined by measuring the relative change in [O] as the carrier gas flow rate, and therefore the flight time, was varied at constant pressure. The change in [O] was monitored by adding NO downstream and measuring the relative intensity of the chemiluminescence (at $\lambda > 550$ nm) from the reaction between NO and O.

Materials: N_2 (99.9999%, Air products), O_2 (99.999%, Air products), CO_2 (99.995%, BOC gases) and CO (99.5% pure, Argo International) were used without further purification. He (99.999%, BOC gases) was passed through a trap containing molecular sieve at 77 K before entering the flow tube. NO (99.95%, Air products) and H_2O were purified via 3 freeze-pump-thaw cycles before dilution in He. The Ni rod (99.99% purity) was obtained from Alfa Aesar.

3. Results

3.1 Recombination reactions

Since the kinetics of these reactions are comparatively straightforward to study, we discuss them first. The depletion in Ni^+ was measured in the presence and absence of the reactant of interest, designated here as X. For the generalised three body reaction

$$Ni^+ + X\ (+M) \rightarrow Ni^+.X \qquad \text{(R10)}$$

a plot of $\ln\left(\frac{[Ni^+]_X^t}{[Ni^+]_0^t}\right)$ vs. reaction time t yields the pseudo first-order rate coefficient k'. Here, $[Ni^+]_X^t$ is the Ni^+ signal at the detector at time t in the presence of reactant X, and $[Ni^+]_0^t$ is the Ni^+ signal in the absence of X. Note that the contact time t is measured directly from the arrival time of the Ni^+ pulses at the mass spectrometer.[15]

Figure 2 shows examples of these kinetic plots for R7 ($Ni^+ + O_2$). Typical Ni^+ concentrations in the upstream section of the tube are estimated at ~5×10^6 cm^{-3}, whereas [X] is > 1×10^{11} molecule cm^{-3}, and the linearity of these plots confirms the assumption of pseudo first-order conditions i.e., [X] is orders of magnitude larger than $[Ni^+]$, so the rate equation can be written as $d[Ni^+]/dt = -k'\,[Ni^+]$, where $k' = k_X[X]$ is effectively constant (k_X is the second-

order rate coefficient of R10). The advantage of using this method is that k' can be determined without needing to know the rate of loss of Ni^+ to the tube walls (k_{diff}).[15, 16]

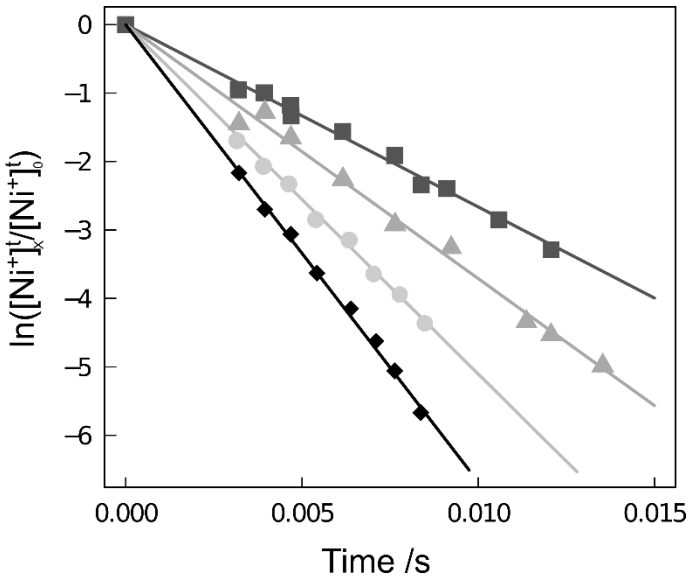

Figure 2. Plot of $\ln\left(\frac{[Ni^+]_X^t}{[Ni^+]_0^t}\right)$ against reaction time for $[O_2] = 1.5 \times 10^{14}$ molecule cm^{-3} (dark grey squares), 5.5×10^{14} molecule cm^{-3} (grey triangles), 1.1×10^{15} molecule cm^{-3} (light grey circles), 2.2×10^{15} molecule cm^{-3} (black diamonds). Conditions: 2.5 Torr, 294 K. The lines are exponential fits through the experimental data, the slopes of which yield k'.

Plots of k' versus [X] yield the second-order rate coefficients. These are plotted as a function of [He] in Figure 3, and the slopes of these plots produce the third-order rate coefficients listed in Table 1. The 1σ uncertainties are computed from the standard errors of the slopes of the regression lines, combined with the uncertainty in the reactant concentrations.

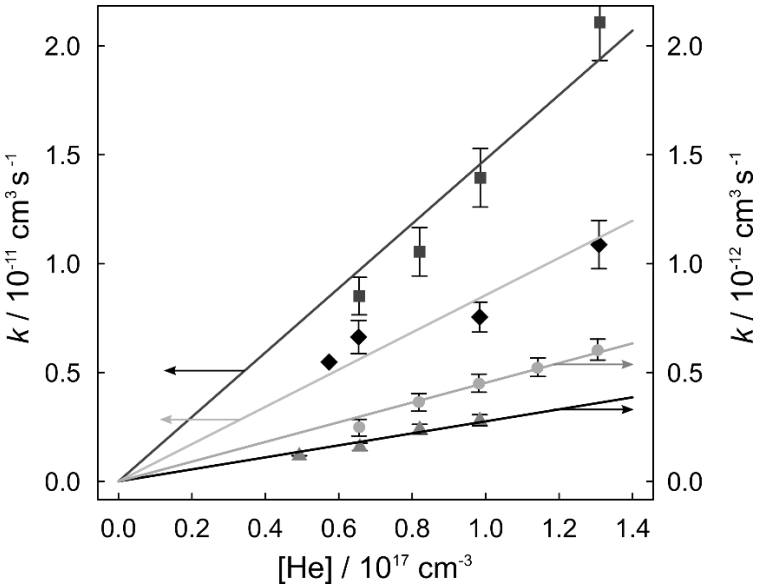

Figure 3. Recombination rate coefficients plotted as a function of pressure, in terms of He concentration. Dark grey squares: R6 ($Ni^+ + H_2O$); black diamonds: R9 ($Ni^+ + CO_2$); grey

circles: R8 ($Ni^+ + N_2$); grey triangles: R7 ($Ni^+ + O_2$). Note the two different ordinates: left hand ordinate for reactions R6 and R9; right hand ordinate for R7 and R8 (indicated with arrows). T = 294 K. The lines are linear regression fits through the experimental data, the slopes of which yield the 3rd order rate coefficients.

Table 1. Summary of reaction rate coefficients measured in the present study (T = 294 K).

No.	Reaction	Rate coefficient [a, b]
R1	$Ni^+ + O_3 \rightarrow NiO^+ + O_2$	$(9.7 \pm 2.1) \times 10^{-10}$
R2a	$NiO^+ + O_3 \rightarrow Ni^+ + 2O_2$	$(7.8 \pm 2.9) \times 10^{-11}$
R2b	$NiO^+ + O_3 \rightarrow NiO_2^+ + O_2$	$(1.9 \pm 0.7) \times 10^{-10}$
R3a	$NiO_2^+ + O_3 \rightarrow NiO^+ + 2O_2$	$(4.6 \pm 2.2) \times 10^{-11}$
R3b	$NiO_2^+ + O_3 \rightarrow ONiO_2^+ + O_2$	$(2.4 \pm 1.2) \times 10^{-10}$
R4	$NiO^+ + O \rightarrow Ni^+ + O_2$	$(1.7 \pm 1.2) \times 10^{-10}$
R5	$NiO^+ + CO \rightarrow Ni^+ + CO_2$	$(7.4 \pm 1.3) \times 10^{-11}$
R6	$Ni^+ + N_2$ (+He) $\rightarrow Ni^+.N_2$	$(3.5 \pm 0.5) \times 10^{-30}$
R7	$Ni^+ + O_2$ (+He) $\rightarrow Ni^+.O_2$	$(2.8 \pm 0.5) \times 10^{-30}$
R8	$Ni^+ + CO_2$ (+He) $\rightarrow Ni^+.CO_2$	$(7.7 \pm 1.0) \times 10^{-29}$
R9	$Ni^+ + H_2O$ (+He) $\rightarrow Ni^+.H_2O$	$(1.3 \pm 0.2) \times 10^{-28}$
R11	$NiO^+ + H_2O \rightarrow NiO^+.H_2O$	$(6.2 \pm 3.0) \times 10^{-10}$
R12	$Ni^+.N_2 + O \rightarrow NiO^+ + N_2$	$(7 \pm 4) \times 10^{-12}$

[a] Units for bimolecular reactions: cm^3 $molecule^{-1}$ s^{-1}. Units for termolecular reactions: cm^6 $molecule^{-2}$ s^{-1}. [b] The stated errors are 1σ.

3.2 The reaction $Ni^+ + O_3$

Measurements of the pseudo first-order reaction of Ni^+ with O_3 (R1) initially gave a lower than expected rate coefficient of ~3×10^{-10} cm^3 $molecule^{-1}$ s^{-1}, as shown in Figure 4 (experimental points are shown as grey diamonds). Given that the analogous systems $Fe^+ + O_3$ [20] and $Al^+ + O_3$ [15]) exhibit significant recycling of the metal oxide ion back to the atomic ion through reaction with O_3, it seemed likely that the same recycling was happening via $NiO^+ + O_3$ (reaction R2a). We therefore added a constant concentration of H_2O into the flow tube to prevent recycling of NiO^+ by R2a, since the recombination reaction

$NiO^+ + H_2O$ (+ M) $\rightarrow$ $NiO^+.H_2O$ $\quad \Delta H^{\ominus} = -212$ kJ mol^{-1} (R11a)

was calculated to be close to its high pressure limit at the pressure of 1 Torr He in the flow tube (details of the theoretical methods used in this calculation are provided in Section 4). It should be noted that the bimolecular reaction

$NiO^+ + H_2O \rightarrow NiOH^+ + OH$ $\quad \Delta H^{\ominus} = +22$ kJ mol^{-1} (R11b)

is too endothermic calculated at the B3LYP/aug-cc-pVQZ level of theory. In fact, taking the experimental values for $D_0(Ni^+\text{-}OH) = 235 \pm 19$ kJ mol^{-1} [11] and $D_0(Ni^+\text{-}O) = 257 \pm 19$ kJ mol^{-1} [12] indicates that the reaction may be significantly more endothermic, $\Delta H^{\ominus} = +(92 \pm 27)$ kJ mol^{-1}. Furthermore, rearrangement of the $NiO^+.H_2O$ to yield the di-hydroxide ion

$$NiO^+.H_2O \rightarrow Ni(OH)_2^+ \qquad \Delta H^{\ominus} = +13 \text{ kJ mol}^{-1} \qquad \text{(R11c)}$$

is also exothermic has a barrier of 128 kJ mol^{-1} with respect to $NiO^+ + H_2O$, so only reaction channel R11a would be important for removing NiO^+ and hence preventing its reaction with O_3. As shown in Figure 4, k' increased significantly in the presence of H_2O (black triangles), consistent with O_3 recycling being shut down. However, a linear fit of k' vs. $[O_3]$ does not go through the origin and obvious curvature can be seen in the plot. This suggests that the H_2O does not completely prevent recycling of NiO^+ to Ni^+ when $[O_3] > 1 \times 10^{12}$ molecule cm^{-3} (this is unavoidable because there is an upper limit to the amount of H_2O that can be added, constrained by its vapour pressure at 293 K). We therefore developed a full kinetic model to fit k_1, k_2, k_3 and k_{11} to the measured data from different experiments.

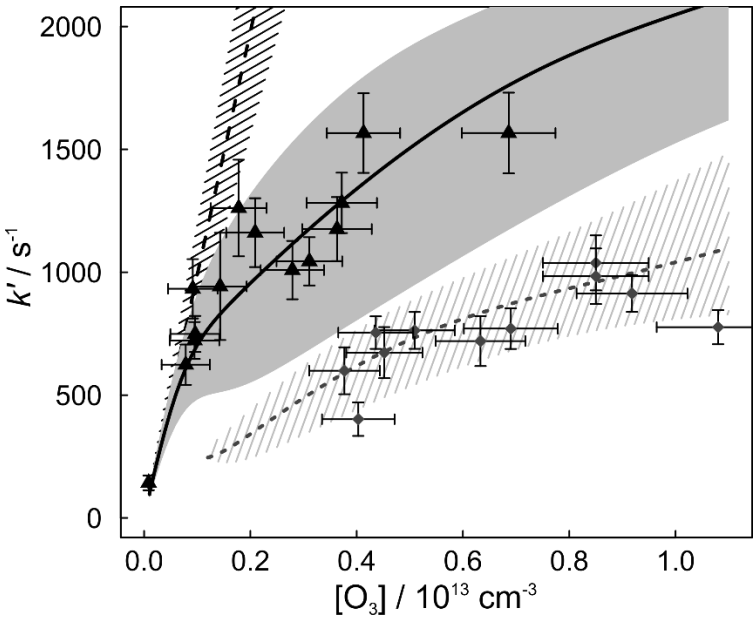

Figure 4. k' for reaction 1 plotted as a function of $[O_3]$, for 3 cases: a) $Ni^+ + O_3$ with full recycling of NiO^+ by reaction R2a (grey diamonds are measurements, dotted line is the model fit, extrapolated to $[O_3] = 0$ with the sparse dotted line); b) $Ni^+ + O_3$ with added $[H_2O] = 3 \times 10^{12}$ cm^{-3}, which reduced the recycling of NiO^+) (black triangles are measurements, black solid line is the model fit); and c) the limiting case of $Ni^+ + O_3$ with no recycling by R2a (black dashed line). The shaded regions correspond to the model fits ± 1σ. Conditions: 1.0 Torr, 294 K.

3.2.1 Flow tube model

The model was developed to describe both the gas-phase reactions of the ions and their loss on the flow tube walls. The wall loss rate for each ion was computed from its diffusion coefficient in He: [21]

$$D = \frac{k_B T}{2.21 n \pi \mu} \sqrt{\frac{\mu}{\alpha e^2}} \quad \text{(E1)}$$

and the wall loss rate is then given by

$$k_{\text{diff}} = D \frac{5.81}{Pr^2} \quad \text{(E2)}$$

where P is pressure, r is the radius of the flow tube, T is temperature, μ is the reduced mass of the ion and He, α is the polarizability of He, e is the charge, and n is the He concentration.[19] k_{diff} for Ni^+, NiO^+ and NiO_2^+ is then 661, 656 and 653 s^{-1}, respectively, at 1 Torr and 294 K. The coupled Ordinary Differential Equations (ODEs) E3 to E5, which describe the wall losses and gas-phase chemistry of Ni^+, NiO^+ and NiO_2^+, were then solved numerically using a 4th-order Runge-Kutta algorithm:

$$\frac{d[Ni^+]}{dt} = k_{2a}[NiO^+][O_3] - \left(k_{\text{diff}}^{Ni^+} + k_1[O_3] + k_9[H_2O][He] + k_7[O_2][He]\right)[Ni^+] \quad \text{(E3)}$$

$$\frac{d[NiO^+]}{dt} = k_1[Ni^+][O_3] + k_{3a}[NiO_2^+][O_3] - \left(k_{\text{diff}}^{NiO^+} + (k_{2a} + k_{2b})[O_3] + k_{11}[H_2O][He] + k_{14}[O_2][He]\right)[NiO^+] \quad \text{(E4)}$$

$$\frac{d[NiO_2^+]}{dt} = k_{2b}[NiO^+][O_3] + k_7[Ni^+][O_2] - \left(k_{\text{diff}}^{NiO_2^+} + (k_{3a} + k_{3b})[O_3]\right)[NiO_2^+] \quad \text{(E5)}$$

The model was designed to replicate the experimental conditions in the flow tube as closely as possible. k' was calculated by sampling the model output (i.e. the concentration of Ni^+ versus t) at 3.75 and 5.00 ms, which were the reaction times set by varying the distance from the sliding injector to the skimmer cone of the mass spectrometer. These times were chosen because the Ni^+ decay was observed to be first-order over this time interval, apart from at low O_3 concentrations (< 10^{12} cm^{-3}) in the absence of H_2O. The modelled k' values were then compared with the experimental data, for experiments both with and without H_2O (solid and dotted lines in Figure 4). Also included in Figure 4 is the case where the only reaction is $Ni^+ + O_3 \rightarrow$ products i.e. with no recycling by reaction R2a. This results in the dashed straight line which passes through the steepest part of the curve of the experimental data when H_2O is added.

The model was fitted to the experimental data both manually and using a Monte Carlo method. The rate coefficient for $Ni^+ + O_3$, k_1, was increased until the initial steep part of the curve matched the experimental data, where reaction 11 with H_2O effectively shuts down the recycling of NiO^+. Combining the fitted k_1 here with similar fits obtained in the experiments on $NiO^+ + CO$ (R4) and $NiO^+ + O$ (R5) (see sections 3.3 and 3.4), yields $k_1(294\ K) = (9.7 \pm 2.1) \times 10^{-10}$ cm^3 $molecule^{-1}$ s^{-1}. The second-order rate coefficient for $NiO^+ + H_2O$ at 1Torr was $(6.2 \pm 3.0) \times 10^{-10}$ cm^3 $molecule^{-1}$ s^{-1}, which is in good agreement with the theoretical estimate in Section 4.

If significant recycling of higher NiO_x^+ (x = 2, 3 …) through reaction with O_3 occurs, then the model fits to the data with and without H_2O became much poorer. The best fits were obtained with only (16 ± 10%) of NiO_2^+ recycling to NiO^+ through R3, and (29 ± 14)% of NiO^+ recycling to Ni^+ through R2. The uncertainties in the rate coefficients k_{2a}, k_{2b}, k_{3a} and k_{3b} were estimated by fitting each data point in turn and determining the mean and standard deviation of the fitted values (Table 1).

3.3 Reaction of NiO^+ with CO

R5 was studied by injecting CO a distance 5 mm upstream of the fixed point where O_3 was introduced into the carrier gas flow. In order to extract k_5, the ratio of [CO]/[O_3] was varied. The recycling of Ni^+ was modelled using the rate coefficients and branching ratios for R1 – R3 that were fitted in Section 3.2. Figure 5 shows the fractional recovery in Ni^+ signal (where 0 is the Ni^+ concentration when [CO] = 0) recovery in Ni^+ signal as a function of the ratio [CO]/[O_3]. As this ratio increases, the percentage recovery starts to plateau around 75%, evident in both the experimental and modelled data. k_5 was obtained by fitting the model to each data point in Figure 5 separately. The resulting mean and standard deviation of the fitted values yields k_5(294 K) = (7.4 ± 1.3) × 10^{-11} cm^3 $molecule^{-1}$ s^{-1}.

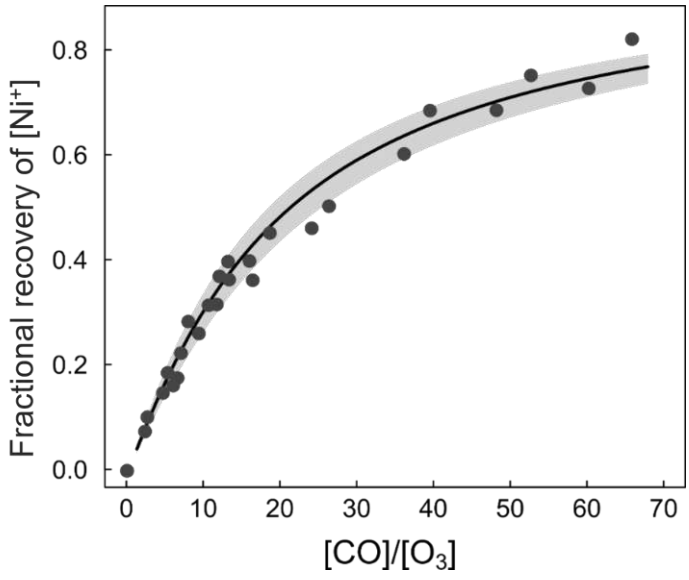

Figure 5. The fractional recovery in [Ni^+] (where 0 is the Ni^+ concentration when [CO] = 0), as a function of [CO]/[O_3]. The solid points are experimental data, and the solid black line is the model fit with the ±1σ uncertainty shown by the shaded region. Conditions: 1 Torr, 294 K.

3.4 Reaction of NiO^+ with O

The reaction of O with NiO^+ recycles Ni^+, so in the presence of O_3 (needed to make NiO^+ via R1) the increase in [Ni^+] when O is injected can be used to obtain k_4. In practice, since it is easier to keep [O] constant with an accurately measured concentration and wall loss rate (see

Section 2), the change in Ni^+ signal was measured for a range of $[O_3]$. The O concentration in the example plot in Figure 6 was maintained at 9.2×10^{12} molecule cm^{-3}. The recycling of Ni^+ was modelled using the rate coefficients and branching ratios for R1 – R3 from Section 3.2, and the measured wall loss of O (470 ± 65 s^{-1}).

The atomic O is generated from the microwave discharge of N_2 (Section 2). This meant that a significant fraction (~8%) of the total flow in the reaction zone was N_2, which led to the formation of $Ni^+.N_2$ through reaction R6. This ion then ligand-switches with O:

$$Ni^+.N_2 + O \rightarrow NiO^+ + N_2 \qquad \Delta H^{\ominus} = -112 \text{ kJ mol}^{-1} \qquad \text{(R12)}$$

In fact, at the low end of the O_3 concentration range (see Figurer 6), the $Ni^+ + N_2$ reaction was faster than $Ni^+ + O_3$, so that $Ni^+.N_2$ became a significant reservoir species. The flow tube model was modified by adding the rate of R4 ($NiO^+ + O$) to ODEs E3 and E4, and inserting an additional ODE to describe the formation and removal of $Ni^+.N_2$ through R6 and R12, respectively. An independent fit of k_4 and k_{12} was then made to each data point in Figure 6. The resulting mean and standard deviation of the fitted values yields $k_4(294\text{ K}) = (1.7 \pm 1.2) \times 10^{-10}$ cm^3 $molecule^{-1}$ s^{-1}, and $k_{12}(294\text{ K}) = (7 \pm 4) \times 10^{-12}$ cm^3 $molecule^{-1}$ s^{-1}. Note that if k_{12} was faster than 7×10^{-12} cm^3 $molecule^{-1}$ s^{-1} then significantly more NiO^+ would be produced in the absence of O_3 than is observed. Indeed, the NiO^+ measurements indicate that k_{12} is probably closer to the lower end of the stated uncertainty.

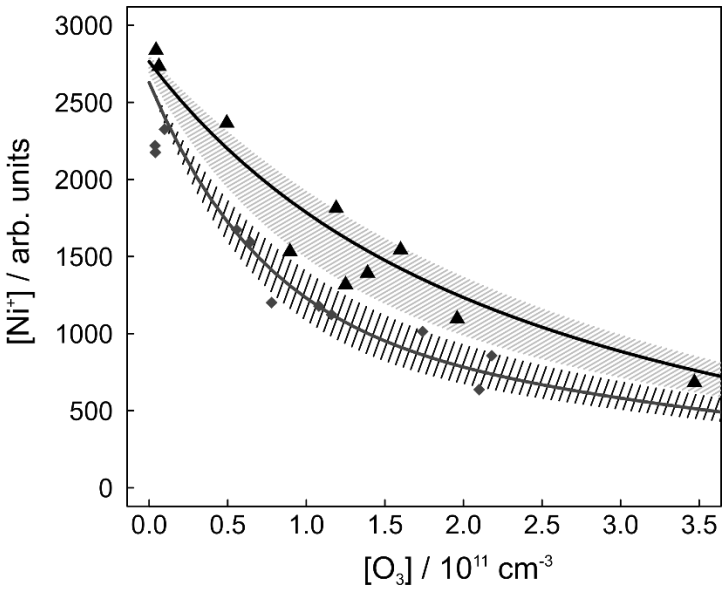

Figure 6. $[Ni^+]$ as a function of $[O_3]$, showing the increased recycling of Ni^+ in the presence of O. When $[O] = 9.2 \times 10^{12}$ molecule cm^{-3}, the experimental points (black triangles) and model fit (black line) should be compared with the experimental points (grey diamonds) and model fit (grey line) in the absence of O. The shades envelopes depict the $\pm 1\sigma$ uncertainties of the model fits. Conditions: 1 Torr, 294 K, $[N_2] = 3.0 \times 10^{15}$ cm^{-3}.

4. Discussion

A set of electronic structure calculations was performed to understand the experimental results and extrapolate to the conditions of planetary mesospheres. The geometries of the NiO_n^+ (n = 1 to 3) ions, and the Ni^+ cluster ions were first optimized at the B3LYP/aug-cc-pVQZ level of theory (Dunning's quadruple-zeta correlation consistent basis set with added diffuse functions) within the Gaussian 16 suite of programs.[22] The resulting geometries are shown in Figure 7, and the Cartesian coordinates, rotational constants and vibrational frequencies are listed in Table 2. Note that the cluster bond energies decrease in the order H_2O > N_2 > CO_2 > O_2. The NiO^+ bond energy of 225 kJ mol^{-1} compares well with values of 230 kJ mol^{-1} [23] and 233 kJ mol^{-1} [24] determined in high level *ab initio* studies using the Multi-Reference Configuration Interaction method. Note that these values for the bond energy are lower than the most recent experimental value of 257 ± 19 kJ mol^{-1}.[12] Our calculated bond energy for Ni^+-OH of 252 kJ mol^{-1} agrees well with previous theoretical estimates of 250 kJ mol^{-1} [25] and 261 kJ mol^{-1},[26] and is within error of the measured $D_0(Ni^+\text{-OH})$ = 235 ± 19 kJ mol^{-1}.[11] The Ni^+-N_2 bond energy of 112 kJ mol^{-1} is somewhat higher than a value of 99 kJ mol^{-1} published in 1989 by Bauchlicher et al.[27] Our value for the Ni^+-O_2 bond energy of 75 kJ mol^{-1} is very close to an earlier estimate of 68 kJ mol^{-1} by Jarvis *et al*.[28] Comparing with the available experimental values discussed above, and taking account of a study comparing density functional methods for calculating bond energies of 3d-transition metal diatomics,[29] we assign an uncertainty of ± 35 kJ mol^{-1} to the bond energies of the Ni-containing ions calculated in the present study.

It should be mentioned at this point that laser ablation of the Ni rod could also produce Ni^+ in the excited ^{4}F state, which is 100.4 kJ mol^{-1} above the $Ni^+(^2D)$ ground state.[13] Both states would be observed as Ni^+ by the mass spectrometer. The role of this excited state has been considered in previous work by Koyanagi *et al.*,[30] since $Ni^+(^4F)$ is radiatively very long-lived[13] and its rate of quenching by He is not known. However, in our experiment $Ni^+(^4F)$ would need to survive > 5 × 10^4 collisions with He before reaching the reaction zone in the flow tube, and there was no evidence of any unexpected change in kinetic behaviour when the He pressure was changed by a factor of 4.

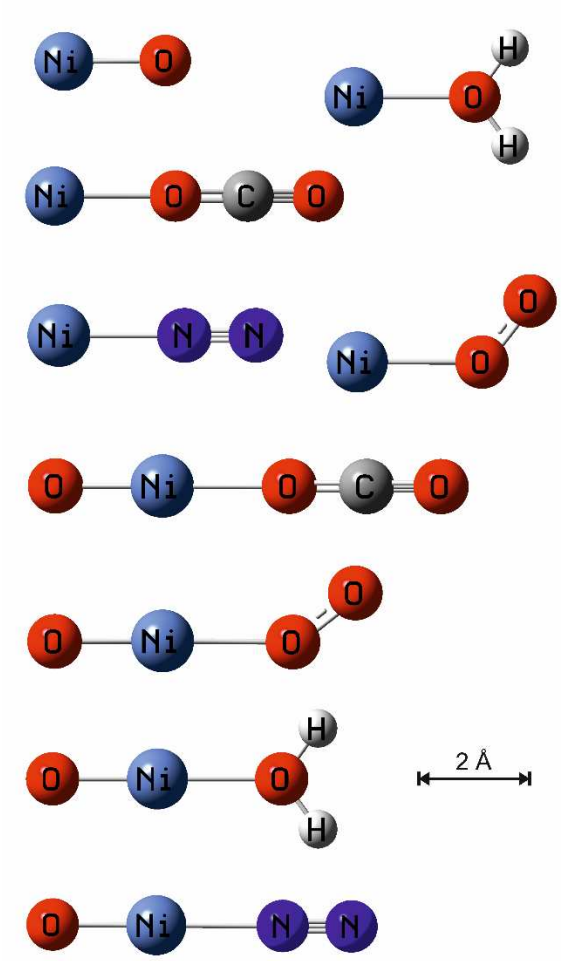

Figure 7. Geometries of NiO^+, $Ni^+.H_2O$, $Ni^+.CO_2$, $Ni^+.N_2$, NiO_2^+, $NiO^+.CO_2$, $ONiO_2^+$, $NiO^+.H_2O$ and $NiO^+.N_2$ ions calculated at the B3LYP/aug-cc-pVQZ level of theory.[22]

4.1 $Ni^+ + O_3$, $NiO^+ + O_3$, $NiO^+ + CO$, and $NiO^+ + O$

Reaction R1 ($Ni^+ + O_3$) is fast, with $k_1(294\ K) = (9.7 \pm 2.1) \times 10^{-10}$ cm^3 molecule^{-1} s^{-1}. The reaction, which is spin conserved on a doublet surface, is about 20% faster than the Langevin capture rate of 8.1×10^{-10} cm^3 molecule^{-1} s^{-1} (although within the experimental error). This probably indicates that the modest dipole moment of O_3 (0.53 D [31]) enhances its capture by Ni^+. The effect of the charge-permanent dipole interaction can be estimated using the formalism of Su and Chesnavich [32], which is derived from trajectory calculations. This yields $k_1(294\ K) = 9.8 \times 10^{-10}$ cm^3 molecule^{-1} s^{-1}, in excellent agreement with the measured value. The statistical adiabatic channel model of Troe [33] with a rotational constant for O_3 of 0.428 cm^{-1} (the geometric mean of the rotation constants for rotation orthogonal to the C_{2v} axis of the molecule along which the dipole lies), yields a slightly higher value of $k_1(294\ K) = 1.1 \times 10^{-9}$ cm^3 molecule^{-1} s^{-1}, still well within the error of the measured value. Both methods predict slightly negative temperature dependences for the reaction which, combined with the experimental value at 294 K yields: $k_1(100 - 300\ K) = 9.7 \times 10^{-10} (T/300)^{-0.16}$ cm^3 molecule^{-1} s^{-1}.

373

374 **Table 2.** Molecular properties and ion-ligand bond energies of the NiO^+, $Ni^+.CO_2$, $Ni^+.H_2O$,
375 $Ni^+.N_2$, NiO_2^+, $ONiO_2^+$, $NiO^+.N_2$, $NiO^+.CO_2$, and $NiO^+.H_2O$ ions (illustrated in Figure 7).

Molecule	Geometry (Cartesian co-ordinates in Å) [a]	Rotational constants (GHz) [a]	Vibrational frequencies (cm^{-1}) [a]	D_0(0 K) (kJ mol^{-1}) [a]
Ni-O^+ ($^4\Sigma^-$)	Ni, 0.0, 0.0, 0.0 O, 0.0, 0.0, 1.637	15.042	707	225 [b]
Ni^+-CO_2 ($^2\Sigma$)	Ni, 0.0, 0.0, 0.132 O, 0.0, 0.0, 2.093 C, 0.0, 0.0, 3.268 O, 0.0, 0.0, 4.408	1.7623	30 (×2), 272, 628 (×2), 1399, 2460	109
Ni^+-H_2O ($^2B_1$)	Ni, -0.006, -0.021, 0.055 O, 0.030, 0.112, 1.985 H, 0.797, -0.052, 2.549 H, -0.716, 0.353, 2.549	409.21 9.1211 8.9222	304, 417, 588, 1645, 3744, 3822	168
Ni^+-N_2 ($^2\Sigma$)	Ni, 0.0, 0.0, 0.126 N, 0.0, 0.0, 2.041 N, 0.0, 0.0, 3.132	4.1199	239 (×2) 343, 2434	112
Ni^+-O_2 ($^2A''$)	Ni, -0.302, 0.968, 0.0 O, 0.623, -1.727, 0.0 O, -0.322, -0.974, 0.0	109.27 4.1414 3.9902	159, 325, 1571	75
ONi^+-O_2 (^2A)	Ni,0,-0.0659, 0.984, -0.184 O, -0.034, -0.774, 0.711 O, -0.013, -1.269, 1.805 O, -0.094, 2.430, -0.945	142.98 2.3051 2.2685	79, 143, 287, 702, 1620	81
ONi^+-N_2 ($^4\Sigma$)	Ni, 0.0, 0.0, 0.959 O, 0.0, 0.0, 2.601 N, 0.0, 0.0, -2.135 N, 0.0, 0.0, -1.046	0.07891	87 (×2), 250 (×2), 308, 692, 2459	111
ONi^+-CO_2 ($^4\Sigma$)	Ni, 0.017, -0.954, 0.0 O, 0.025, -2.580, 0.0 C, 0.003, 2.167, 0.0 O, -0.003, 3.303, 0.0 O, 0.008, 0.987, 0.0	1.2461	32 (×2), 119 (×2), 287, 627 (×2), 751, 1400, 2462	134
ONi^+-H_2O ($^4A_2$)	Ni, 0.161, 0.0, 0.0 O, 1.791, 0.0, -0.0 O, -1.772, -0.0, 0.0 H, -2.337, -0.785, 0.0 H, -2.339, 0.785, 0.0	407.60 4.4435 4.3956	113, 136, 299, 444, 639, 706, 1662, 3728, 3801	212

376 [a] Calculated at the B3LYP/aug-cc-pVQZ level of theory [22]

377 [b] Dissociation to $Ni^+(^2D)$ + $O(^3P)$

Reaction R1 is exothermic by 125 kJ mol^{-1}, and so NiO^+ could be produced in 9 low-lying electronic states (3 of quartet spin multiplicity and 6 doublet states), in addition to the $NiO^+(X^4\Sigma^-)$ ground state.[23] When using the flow tube model to determine rate coefficients for NiO^+ reactions, we have to assume that the NiO^+ is largely produced in the ground state or else is quenched sufficiently rapidly in 1 Torr of He. The rate coefficient for the reaction between NiO^+ and O_3, k_2, is about 35% of its Langevin capture rate. Both channels of the reaction are quite exothermic (Section 1); the more exothermic channel producing $NiO_2^+ + O_2$ has a higher branching ratio (f_{2b} = 71%). For comparison, the branching ratio to produce FeO_2^+ from the analogous reaction $FeO^+ + O_3$ is 39%,[20] and to produce MgO_2^+ from $MgO^+ + O_3$ is 65%.[18] In the case of reaction R3 between NiO_2^+ and O_3, once again the more exothermic channel producing $ONiO_2^+ + O_2$ (Section 1) has the higher branching ratio (f_{3b} = 84%). In contrast, for the reaction $FeO_2^+ + O_3$ the channel producing $FeO_3^+ + O_2$ is close to thermoneutral, and the branching ratio is only 21%.[20]

Reaction 1 has been studied previously by McDonald *et al.*[34] in a selected-ion flow tube. They measured $k_1(300 – 500\ K) = (11 \pm 2) \times 10^{-10}$ cm^3 molecule^{-1} s^{-1}, which is in very good agreement with the present study. McDonald *et al.*[34] showed that recycling of NiO^+ by O_3 (reaction 2a) had been neglected in an earlier study[35] which reported a 40% smaller value for k_1. Again, this is consistent with the present finding, and the measured branching ratios f_{2a} = (29 ± 14)% from the present study and (40 ± 20)% from McDonald *et al.*[34] agree within error. However, k_2 from the present study is $(2.7 \pm 0.8) \times 10^{-10}$ cm^3 molecule^{-1} s^{-1}, which is outside the uncertainty of the value $(9.5 \pm 3.0) \times 10^{-10}$ cm^3 molecule^{-1} s^{-1} from McDonald *et al.*[34] In the case of reaction R3 between NiO_2 and O_3, $k_3 = (2.9 \pm 1.2) \times 10^{-10}$ cm^3 molecule^{-1} s^{-1} from the present study, which agrees within error with the value of $(10 \pm 7) \times 10^{-10}$ cm^3 molecule^{-1} s^{-1} from McDonald *et al.*,[34] although our value of f_{3a} = (16 ± 10)% is lower than their estimate of the branching ratio lying between 45 and 95%. If we put the rate coefficients for R1 – R3, including the branching ratios for R2 and R3, from McDonald *et al.*[34] into our flow tube model, we can model our data in Figure 4 when H_2O is added (black diamonds), which is expected because of the very good agreement of k_1; however, in the absence of H_2O the k' modelled values as a function of O_3 are significantly higher than the experimental (grey diamonds in Figure 4), even within the error of the rate coefficients.

The rate coefficient for $NiO^+ + O$ is $k_4(294\ K) = (1.7 \pm 1.2) \times 10^{-10}$ cm^3 molecule^{-1} s^{-1}, which is 29% of the Langevin capture rate. This reaction can occur on doublet and sextet surfaces, and is exothermic enough to produce excited products: $Ni^+(^4F) + O_2(X^3\Sigma_g^-)$ (exothermic by 184 kJ mol^{-1}), or $Ni^+(^2D) + O_2(a^1\Delta_g)$ (exothermic by 190 kJ mol^{-1}). The rate coefficient is significantly faster than the analogous reactions of FeO^+ ($(3.2 \pm 1.5) \times 10^{-11}$ cm^3 molecule^{-1} s^{-1} [19]) and CaO^+ ($(4.2 \pm 2.8) \times 10^{-11}$ cm^3 molecule^{-1} s^{-1} [17]), although not as fast as $MgO^+ + O$ ($(5.9 \pm 2.4) \times 10^{-10}$ cm^3 molecule^{-1} s^{-1} [36]).

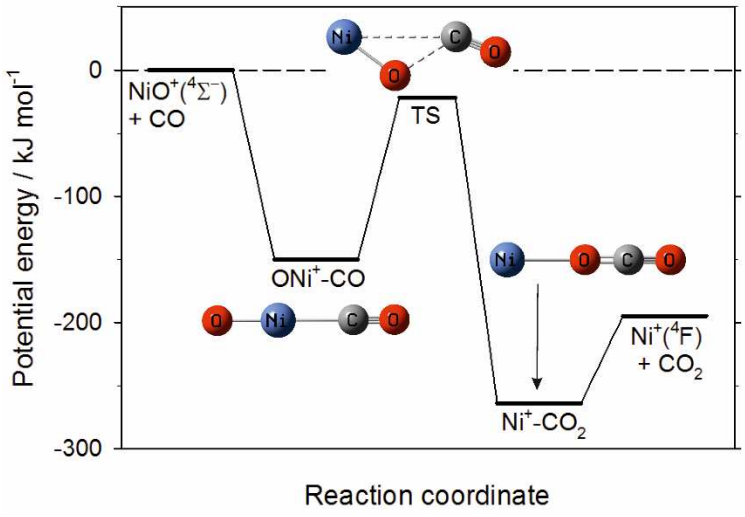

Figure 8. Potential energy surface of quartet spin multiplicity for reaction 5, $NiO^+ + CO$, calculated at the B3LYP/aug-cc-pVQZ level of theory.

The rate coefficient for $NiO^+ + CO$ is $k_5(294\ K) = (7.4 \pm 1.3) \times 10^{-11}$ cm^3 molecule^{-1} s^{-1}, which is somewhat slower than the analogous reactions of CO with FeO^+ ($(1.59 \pm 0.34) \times 10^{-10}$ cm^3 molecule^{-1} s^{-1} [19]), CaO^+ ($(2.8 \pm 1.5) \times 10^{-10}$ cm^3 molecule^{-1} s^{-1} [17]) and MgO^+ ($(3.2 \times 10^{-10}$ cm^3 molecule^{-1} s^{-1}). Since the ground state of NiO^+ is $^4\Sigma^-$, if this reaction conserves spin then Ni^+ will be produced in the low-lying ^{4}F state. Figure 8 is a plot of the quartet potential energy surface for the reaction, calculated at the B3LYP/aug-cc-pVQZ level.[22] This shows that the CO first binds to the Ni, then the O atom (originally from NiO^+) rotates around the Ni to form $Ni^+.CO_2$ (quartet spin multiplicity), before dissociating to $Ni^+(^4F) + CO_2$. The transition state is calculated to be only 21 kJ mol^{-1} below the energy of the reactant entrance channel. Using the Master Equation Solver for Multi-Energy well Reactions (MESMER) program[37] to calculate k_5 on this potential energy surface, the experimental rate coefficient can be fitted if this barrier is raised by only 7 kJ mol^{-1}, which is within the uncertainty at this level of theory.[29]

4.2 $Ni^+ + N_2$, O_2, CO_2 and H_2O

The rate coefficient for the recombination of Ni^+ with N_2 (k_6) does not appear to have been reported previously, although the formation of the product $Ni^+.N_2$ ion has been reported in a ring electrode trap.[10] The recombination kinetics of Ni^+ with O_2 has been studied in a selected ion flow tube apparatus by Koyanagi *et al.*,[30] who obtained a bimolecular rate coefficient of 2.0×10^{-13} cm^3 molecule^{-1} s^{-1} in 0.35 Torr of He. This equates to a 3rd-order rate coefficient of $k_7 = 1.7 \times 10^{-29}$ cm^6 molecules^{-2} s^{-1}, which is roughly 6 times the value from the present study of $(2.8 \pm 0.5) \times 10^{-30}$ cm^6 molecule^{-2} s^{-1}. The reason for the discrepancy is not clear, and Koyanagi *et al.*[30] did not report a pressure-dependent study of the reaction. The most stable form of the product is bent Ni-O_2^+ with doublet spin multiplicity (Table 2), which is 267 kJ mol^{-1} more stable (at the B3LYP/aug-cc-pVQZ level) than the $ONiO^+$ quartet where the Ni

inserts into the O-O bond. The bimolecular reaction channel, $Ni^+ + O_2 \rightarrow NiO^+ + O$, is endothermic by 284 kJ mol^{-1}, consistent with the measured reaction threshold energy of ~3 eV measured in an ion beam apparatus.[38]

There do not appear to have been any previous studies of the recombination of Ni^+ with CO_2 or H_2O. However, Cheng *et al.* studied the reaction between Ni^+ and D_2O.[39] Their value of 1.7×10^{-12} cm^3 molecule^{-1} s^{-1} in 0.35 Torr He equates to a 3rd-order rate coefficient of 1.5×10^{-28} cm^6 molecule^{-2} s^{-1}, which is slightly higher than our value for H_2O, $k_9 = (1.3 \pm 0.2) \times 10^{-28}$ cm^6 molecules^{-2} s^{-1}. This is expected because the lower vibrational frequencies of D_2O lead to a higher density of states in Ni^+-D_2O than in the Ni^+-H_2O adduct.

The rate coefficients for the recombination reactions R6 – R9 can be extrapolated to temperatures and pressures outside the experimental range by using Rice-Ramsperger-Kassel-Markus (RRKM) theory. Here we use a solution of the Master Equation (ME) based on the inverse Laplace transform method,[40] which we have applied previously to recombination reactions of metallic species.[15, 16, 18, 41, 42] Hence, only a brief description is given here. These reactions proceed via the formation of an excited adduct, which can either dissociate or be stabilized by collision with the third body (He). The internal energy of this adduct was divided into a contiguous set of grains (width 30 cm^{-1}), each containing a bundle of rovibrational states. Each grain was then assigned a set of microcanonical rate coefficients for dissociation, which were determined using inverse Laplace transformation to link them directly to $k_{rec,\infty}$, the high pressure limiting recombination coefficient. In the case of these reactions, $k_{rec,\infty}$ was set to the Langevin capture rate (including a correction for the permanent dipole of H_2O in the case of R9). The density of states of each adduct was calculated with the vibrational frequencies and rotational constants listed in Table 2, using the Beyer-Swinehart algorithm for the vibrational modes (without making a correction for anharmonicity), and a classical densities of states treatment for the rotational modes.[43] For these reactions, the two low-frequency degenerate vibrational modes of Ni^+-N_2 (239 cm^{-1}) and Ni^+-CO_2 (30 cm^{-1}) were treated as 2-dimensional free rotor; for $Ni^+ + O_2$, the low-frequency bending mode (159 cm^{-1}) was treated as 1-D free rotor; and for $Ni^+ + H_2O$, the out-of-plane and in-plane rocking modes of the Ni^+-H_2O cluster (304 and 588 cm^{-1}) were treated as a 2-D rotor. [43]

The probability of collisional transfer between grains was estimated using the exponential down model, where the average energy for downward transitions is designated $\langle \Delta E \rangle_{down}$,[43] and the probabilities for upward transitions are determined by detailed balance. The collision rate of the third body (He) with the adduct was set to the corresponding Langevin capture rate. The ME, which describes the evolution with time of the adduct grain populations, was then expressed in matrix form and solved to yield the recombination rate constant at a specified pressure and temperature. The only adjustable parameter when fitting to the experimental data was the average energy for downward transitions, $\langle \Delta E \rangle_{down}$. Table 3 summarises the results. The fitted values of $\langle \Delta E \rangle_{down}$ lie between 125 and 150 cm^{-1} i.e. within the expected range for He.[43] In fact, the sensitivity of the calculated rate coefficient to $\langle \Delta E \rangle_{down}$ provides a way of assessing the likely uncertainty of the theoretical cluster binding energy. Taking reaction R8 as an example, the theoretical binding energy of Ni^+-CO_2 is 108 kJ mol^{-1}; an uncertainty of ± 15 kJ mol^{-1} would require $\langle \Delta E \rangle_{down}$ to range between 70 and 190 cm^{-1} i.e. somewhat outside the expected range for He,[43] so this is likely an upper limit to the uncertainty in the binding energy.

Table 3. Fitted RRKM parameters and low-pressure limiting rate coefficients for the addition of a single ligand to Ni^+ with He as third body

Reaction	$\langle\Delta E\rangle_{down}$ cm^{-1}	$\log_{10}(k_{rec,0}/\ cm^6\ molecule^{-2}\ s^{-1})$ T = 100 – 600 K	% uncertainty in $k_{rec,0}$ at 180 K
$Ni^+ + N_2$	140	$-27.5009 + 1.0667\log_{10}(T) - 0.74741(\log_{10}(T))^2$	28.6
$Ni^+ + O_2$	130	$-27.8098 + 1.3065\log_{10}(T) - 0.81136(\log_{10}(T))^2$	31.5
$Ni^+ + CO_2$	125	$-29.805 + 4.2282\log_{10}(T) - 1.4303(\log_{10}(T))^2$	27.9
$Ni^+ + H_2O$	150	$-24.318 + 0.20448\log_{10}(T) - 0.66676(\log_{10}(T))^2$	27.9

The temperature dependence of $\langle\Delta E\rangle_{down}$ is typically small and usually described as T^{α}.[43] Here, the parameter α was set to 0.0, and then varied between the expected range of -0.5 and +0.5. The resulting fits of the low pressure limiting rate coefficient, $k_{rec,0}$, through the experimental data points, and extrapolated between 100 and 600 K, are illustrated in Figure 9. The $Ni^+ + H_2O$ reaction is nearly 2 orders of magnitude faster than $Ni^+ + O_2$ (at the same temperature), reflecting the much deeper well and the increased number of atoms in the Ni^+-H_2O cluster, which increases the density of ro-vibrational states of the adduct. $k_{rec,0}$ does not follow a simple T^{-n} dependence, and so a second-order dependence on $\log_{10}T$ was fitted in each case. The resulting expressions are listed in the third column of Table 3 (the large number of significant figures in the fitted polynomial parameters are provided for numerical accuracy). The faint lines in Figure 9 show the sensitivity of the RRKM fit for each reaction when α is varied between -0.5 and +0.5. At a temperature of 180 K (typical of the terrestrial mesosphere[3]), the overall uncertainty in $k_{rec,0}$ obtained by combining the experimental error and RRKM extrapolation is around 30% (last column in Table 3). These low-pressure limiting rate coefficients are appropriate for the meteoric ablation region in a planetary atmosphere where the pressure is less than 10^{-5} bar.

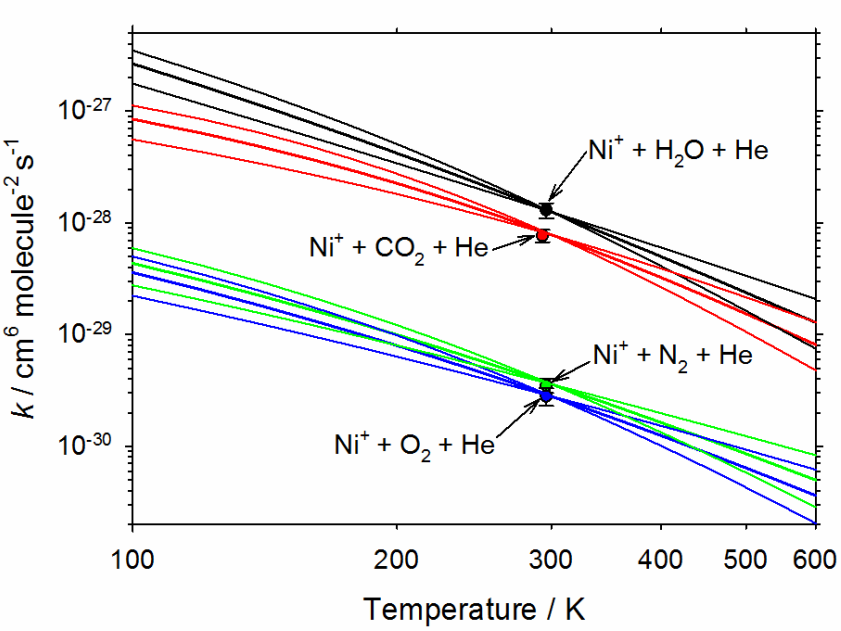

Figure 9. RRKM fits (thick lines) through the experimental data points (solid circles) for the recombination reactions of Ni^+ with N_2 (green), O_2 (blue), CO_2 (red) and H_2O (black). The faint lines indicate the sensitivity of each fit to α, the temperature-dependence of $\langle\Delta E\rangle_{down}$, varying between -0.5 and 0.5.

4.3 Atmospheric Implications

In order to use the recombination reaction rate coefficients for modelling in a planetary atmosphere, the $k_{rec,0}$ values need to be adjusted to account for the relative efficiencies of the major atmospheric species compared with the He used in the kinetic measurements. For N_2 and O_2 acting as a third body in an ion-molecule recombination reaction, the rate coefficients k_6, k_7, k_8 and k_9 should be increased by a factor of 3,[3] and for CO_2 by a factor of 8.[36]

Before examining the relative importance of the NiO^+ reactions, we estimated the rate coefficients for the addition of likely atmospheric species to this ion. These calculations were performed using the RRKM method described in Section 4.2, with the molecular parameters for $ONiO_2^+$, $ONi^+.N_2$, $ONi^+.CO_2$ and $ONi^+.H_2O$ from electronic structure calculations (see Table 2). The resulting rate coefficients between 120 and 300 K are:

$k_{rec,0}(NiO^+ + N_2 + He) = 3.4 \times 10^{-30} (T/300)^{-3.38}$ cm^6 molecule^{-2} s^{-1}

$k_{rec,0}(NiO^+ + O_2 + He) = 1.1 \times 10^{-29} (T/300)^{-3.39}$ cm^6 molecule^{-2} s^{-1}

$k_{rec,0}(NiO^+ + CO_2 + He) = 1.2 \times 10^{-27} (T/300)^{-3.42}$ cm^6 molecule^{-2} s^{-1}

$k_{rec,0}(NiO^+ + H_2O + He) = 2.0 \times 10^{-26} (T/300)^{-2.90}$ cm^6 molecule^{-2} s^{-1}

The expected uncertainty is probably a factor of 3 at 300 K. Note that the second-order recombination rate for $NiO^+ + H_2O$ at 1 Torr and 294 K is 7.2×10^{-10} cm^3 molecule^{-1} s^{-1}, which agrees well with the experimental fit in Section 3.2 (Table 1).

The vertical profiles for the removal rates of Ni^+ and NiO^+ ions in the atmospheres of Earth and Mars are illustrated in Figure 10. In the case of the terrestrial atmosphere, the vertical profiles of *T*, pressure and the mixing ratios of O_3, N_2, CO_2 and H_2O are taken from the Whole Atmosphere Community Climate Model (WACCM4),[44, 45] for the conditions of 40°N in April, at local midnight. Figure 10a shows that reaction with O_3 dominates the removal of Ni^+ between 83 and 110 km (rocket-borne mass spectrometric measurements show that the peak of the Ni^+ occurs between 95 and 105 km [2]). Even during daytime, when the O_3 concentration decreases by around 1 order of magnitude due to photolysis,[3] reaction with O_3 will still dominate over this altitude range. Above 110 km and below 83 km, recombination with N_2 dominates and recombination with O_2 is about a factor of 7 times slower. Formation of $Ni^+.CO_2$ in the terrestrial atmosphere should not be important, not only because direct recombination is uncompetitive (Figure 10a), but also because – unusually - the $Ni^+.N_2$ cluster is more strongly bound than $Ni^+.CO_2$ (Table 2) and so will not ligand-switch with CO_2, unlike other metallic ions such as Mg^+,[18] Al^+,[15] Ca^+,[17] and Fe^+.[16] Recombination of Ni^+ with H_2O is least important because of the low mixing ratio of H_2O (less than a few ppm above 80 km [3]).

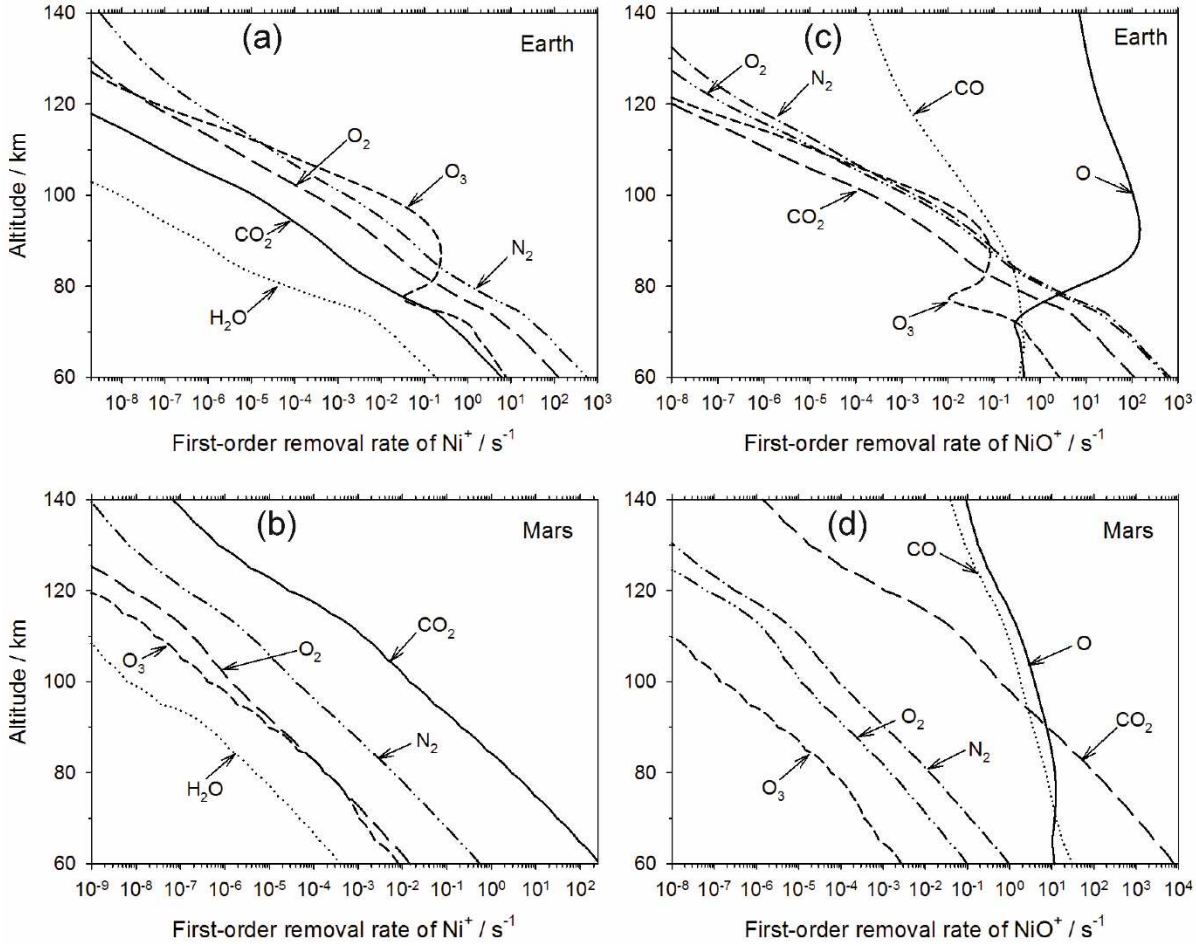

Figure 10. Removal rates of Ni^+ (panels (a) and (b)), and NiO^+ (panels (c) and (d)) in the upper atmospheres of Earth (panels (a) and (c), 40°N, local midnight, April) and Mars (panels (b) and (d), local noon, latitude = 0°, solar longitude L_s = 85°).

For Mars, the vertical profiles of the relevant species and T are taken from the Mars Climate Database v.5.2 (http://www-mars.lmd.jussieu.fr/mcd_python/),[46] for the conditions of latitude = 0°, local noon and solar longitude L_s = 85° (northern hemisphere summer). Because the Martian atmosphere is ~95% CO_2, and the O_3 concentration is much lower than in the terrestrial atmosphere, recombination with CO_2 dominates by over 2 orders of magnitude across the entire range of altitude from 60 to 140 km (Figure 10b).

On Earth, the fast reaction of NiO^+ with O is easily the most important loss process for NiO^+ above 80 km (Figure 10c), so that NiO^+ will have a turnover lifetime of around 10 ms. Below 80 km, recombination with N_2 and O_2 produces the $NiO^+.N_2$ and $ONiO_2^+$ ions, which could then ligand-switch with CO_2 or H_2O as these molecules bind more strongly to NiO^+ (Table 2). Note that any of these cluster ions can react directly with O e.g. for the mostly strongly bound cluster ion

$$NiO^+.H_2O + O \rightarrow NiO_2^+ + H_2O \qquad \Delta H^\ominus = -136 \text{ kJ mol}^{-1} \qquad (13a)$$

$$\rightarrow Ni^+.H_2O + O_2 \qquad \Delta H^\ominus = -240 \text{ kJ mol}^{-1} \qquad (13b)$$

On Mars, the reactions of NiO^+ with O and CO dominate above 90 km (Figure 10d), so that NiO^+ will have a lifetime around 100 ms. At lower altitudes recombination with CO_2 becomes more important, although the resulting $NiO^+.CO_2$ cluster ion will likely then react with O, CO or H_2O.

5. Conclusions

The rate coefficients for the reactions of Ni^+ with O_3, N_2, O_2, CO_2 and H_2O, and the reactions of NiO^+ with O, CO and O_3 have been measured, all but the $Ni^+ + O_2$ reaction apparently for the first time. The reaction of $Ni^+(^2D)$ with O_3 to form $NiO^+(^4\Sigma^-)$ is spin-conserved and quite exothermic, and so proceeds at the ion-molecule capture rate slightly enhanced by the small dipole moment of O_3. This reaction dominates removal of Ni^+ in the terrestrial atmosphere because of the relatively high concentration of O_3 in the tertiary ozone maximum around 87 km. However, the most likely fate of NiO^+ is fast recycling by O atoms to Ni^+. In contrast, on Mars the recombination of Ni^+ with CO_2 is the most rapid removal process by over 2 orders of magnitude, throughout Mars' mesosphere.

Acknowledgements

This work was supported by Natural Environment Research Council grant NE/P001815/1. S.M.D. was supported by a studentship from the NERC SPHERES Doctoral Training Program. The data used in the paper is archived at the Leeds University PetaByte Environmental Tape Archive and Library (PETAL; http://www.see.leeds.ac.uk/business-and-consultation/ facilities/petabyte-environmental-tapearchive-and-library-petal/), is available from J.M.C.P.

Conflicts of interest

There are no conflicts to declare.

References

1. J. M. C. Plane, G. J. Flynn, A. Määttänen, J. E. Moores, A. R. Poppe, J. D. Carrillo-Sánchez and C. Listowski, *Space Sci. Rev.*, 2017, **214**, art. no.: 23.
2. J. D. Carrillo-Sánchez, J. C. Gómez-Martín, D. L. Bones, D. Nesvorný, P. Pokorný, M. Benna and J. M. C. Plane, *Icarus*, 2020, **335**, art. no.: 113395.
3. J. M. C. Plane, W. Feng and E. C. M. Dawkins, *Chem. Rev.*, 2015, **115**, 4497-4541.
4. W. Feng, D. R. Marsh, M. P. Chipperfield, D. Janches, J. Hoeffner, F. Yi and J. M. C. Plane, *J. Geophys. Res.-Atmos.*, 2013, **118**, 9456-9474.
5. R. L. Collins, J. Li and C. M. Martus, *Geophys. Res. Lett.*, 2015, **42**, 665-671.
6. M. Asplund, N. Grevesse, A. J. Sauval and P. Scott, in *Ann. Rev. Astron. Astrophys.*, eds. R. Blandford, J. Kormendy and E. van Dishoeck, Annual Reviews, Palo Alto2009, vol. 47, pp. 481-522.
7. M. Gerding, S. Daly and J. M. C. Plane, *Geophys. Res. Lett.*, 2019, **46**, 408-415.
8. E. Kopp, *J. Geophys. Res.-Space Phys.*, 1997, **102**, 9667-9674.
9. T. P. Mangan, N. McAdam, S. M. Daly and J. M. C. Plane, *J. Phys. Chem. A*, 2019, **123**, 601-610.
10. S. Schlemmer, A. Luca and D. Gerlich, *Int. J. Mass Spectr.*, 2003, **223**, 291-299.
11. P. B. K. Armentrout, B. L. , in *Organometallic Ion Chemistry*, ed. B. S. Freiser, Kluwer AcademicPublisher, Dordrecht1996, pp. 1-45.
12. D. Vardhan, R. Liyanage and P. B. Armentrout, *J. Chem. Phys.*, 2003, **119**, 4166-4178.
13. A. Kramida, Y. Ralchenko, J. Reader and N. A. Team, National Institute of Standards and Technology, Gaithersburg, MD2018.
14. X. Chu, Z. Yu, C. S. Gardner, C. Chen and W. Fong, *Geophys. Res. Lett.*, 2011, **38**, art. no.: L23807.
15. S. M. Daly, D. L. Bones and J. M. C. Plane, *Phys. Chem. Chem. Phys.*, 2019, **21**, 14080-14089.
16. T. Vondrak, K. R. I. Woodcock and J. M. C. Plane, *Phys. Chem. Chem. Phys.*, 2006, **8**, 503-512.

17. S. Broadley, T. Vondrak, T. G. Wright and J. M. C. Plane, *Phys. Chem. Chem. Phys.*, 2008, **10**, 5287-5298.

18. C. L. Whalley, J. C. Gomez Martin, T. G. Wright and J. M. C. Plane, *Phys. Chem. Chem. Phys.*, 2011, **13**, 6352-6364.

19. K. R. S. Woodcock, T. Vondrak, S. R. Meech and J. M. C. Plane, *Phys. Chem. Chem. Phys.*, 2006, **8**, 1812-1821.

20. J. J. Melko, S. G. Ard, T. Le, G. S. Miller, O. Martinez, N. S. Shuman and A. A. Viggiano, *J. Phys. Chem. A*, 2017, **121**, 24-30.

21. M. H. Rees, *Physics and Chemistry of the Upper Atmosphere*, Cambridge University Press, Cambridge, 1989.

22. M. J. Frisch, G. W. Trucks, H. B. Schlegel, G. E. Scuseria, M. A. Robb, J. R. Cheeseman, G. Scalmani, V. Barone, G. A. Petersson, H. Nakatsuji, X. Li, M. Caricato, A. V. Marenich, J. Bloino, B. G. Janesko, R. Gomperts, B. Mennucci, H. P. Hratchian, J. V. Ortiz, A. F. Izmaylov, J. L. Sonnenberg, D. Williams-Young, F. Ding, F. Lipparini, F. Egidi, J. Goings, B. Peng, A. Petrone, T. Henderson, D. Ranasinghe, V. G. Zakrzewski, N. R. J. Gao, G. Zheng, W. Liang, M. Hada, M. Ehara, K. Toyota, R. Fukuda, J. Hasegawa, M. Ishida, T. Nakajima, Y. Honda, O. Kitao, H. Nakai, T. Vreven, K. Throssell, J. J. A. Montgomery, J. E. Peralta, F. Ogliaro, M. J. Bearpark, J. J. Heyd, E. N. Brothers, K. N. Kudin, V. N. Staroverov, T. A. Keith, R. Kobayashi, J. Normand, K. Raghavachari, A. P. Rendell, J. C. Burant, S. S. Iyengar, J. Tomasi, M. Cossi, J. M. Millam, M. Klene, C. Adamo, R. Cammi, J. W. Ochterski, R. L. Martin, K. Morokuma, O. Farkas, J. B. Foresman and D. J. Fox, Gaussian, Inc., Wallingford, CT, USA2016.

23. C. N. Sakellaris and A. Mavridis, *J. Chem. Phys.*, 2013, **138**, art. no.: 054308.

24. Y. Nakao, K. Hirao and T. Taketsugu, *J. Chem. Phys.*, 2001, **114**, 7935-7940.

25. A. Ricca and C. W. Bauschlicher, Jr., *J. Phys. Chem. A*, 1997, **101**, 8949-8955.

26. C. J. Thompson, F. Aguirre, J. Husband and R. B. Metz, *J. Phys. Chem. A*, 2000, **104**, 9901-9905.

27. C. W. Bauschlicher, S. R. Langhoff and L. A. Barnes, *Chem. Phys.*, 1989, **129**, 431-437.

28. M. J. Y. Jarvis, L. F. Pisterzi, V. Blagojevic, G. K. Koyanagi and D. K. Bohme, *Int. J. Mass Spectr.*, 2003, **227**, 161–173.

29. E. R. Johnson and A. D. Becke, *J. Chem. Phys.*, 2017, **146**, arrt. no.: 211105.

30. G. K. Koyanagi, D. Caraiman, V. Blagojevic and D. K. Bohme, *J. Phys. Chem. A*, 2002, **106**, 4581-4590.

31. D. R. Lide, *Handbook of Physics and Chemistry*, CRC Press, Boca Raton, FL, 2006.

32. T. Su and W. J. Chesnavich, *J. Chem. Phys.*, 1982, **76**, 5183-5185.

33. J. Troe, *Chem. Phys. Lett.*, 1985, **122**, 425-430.

34. D. C. McDonald, B. C. Sweeny, S. G. Ard, J. J. Melko, J. E. Ruliffson, M. C. White, A. A. Viggiano and N. S. Shuman, *J. Phys. Chem. A*, 2018, **122**, 6655-6662.

35. A. Bozovic, S. Feil, G. K. Koyanagi, A. A. Viggiano, X. H. Zhang, M. Schlangen, H. Schwarz and D. K. Bohme, *Chem. Europ. J.*, 2010, **16**, 11605-11610.

36. C. L. Whalley and J. M. C. Plane, *Faraday Disc.*, 2010, **147**, 349-368.

37. D. R. Glowacki, C.-H. Liang, C. Morley, M. J. Pilling and S. H. Robertson, *J. Phys. Chem. A*, 2012, **116**, 9545−9560.

38. P. B. Armentrout, L. F. Halle and J. L. Beauchamp, *J. Chem. Phys.*, 1982, **76**, 2449-2457.

39. P. Cheng, G. K. Koyanagi and D. K. Bohme, *J. Phys. Chem. A*, 2007, **111**, 8561-8573.

40. R. De Avillez Pereira, D. L. Baulch, M. J. Pilling, S. H. Robertson and G. Zeng, *J. Phys. Chem.*, 1997, **101**, 9681.

41. S. L. Broadley, T. Vondrak and J. M. C. Plane, *Phys. Chem. Chem. Phys.*, 2007, **9**, 4357-4369.

42. R. J. Rollason and J. M. C. Plane, *Phys. Chem. Chem. Phys.*, 2000, **2**, 2335-2343.

43. R. G. Gilbert and S. C. Smith, *Theory of Unimolecular and Recombination Reactions*, Blackwell, Oxford, 1990.

44. D. R. Marsh, M. J. Mills, D. E. Kinnison, J.-F. Lamarque, N. Calvo and L. M. Polvani, *Journal of Climate*, 2013, **26**, 7372-7391.

45. R. R. Garcia, D. Marsh, D. E. Kinnison, B. Boville, and F. Sassi, *J. Geophys. Res.*, 2007, **112**, D09301.

46. F. Forget, F. Hourdin, R. Fournier, C. Hourdin, O. Talagrand, M. Collins, S. R. Lewis, P. L. Read and J.-P. Huot, *J. Geophys. Res.*, 1999, **104**, 24155-24176.

Figure Captions.

Figure 1. Reaction scheme for the ion-molecule chemistry of Ni^+ in the Earth's mesosphere and lower thermosphere.

Figure 2. Plot of $\ln\left(\frac{[Ni^+]_X^t}{[Ni^+]_0^t}\right)$ against reaction time for $[O_2] = 1.5 \times 10^{14}$ molecule cm^{-3} (dark grey squares), 5.5×10^{14} molecule cm^{-3} (grey triangles), 1.1×10^{15} molecule cm^{-3} (light grey circles), 2.2×10^{15} molecule cm^{-3} (black diamonds). Conditions: 2.5 Torr, 294 K. The lines are exponential fits through the experimental data, the slopes of which yield k'.

Figure 3. Recombination rate coefficients plotted as a function of pressure, in terms of He concentration. Dark grey squares: R6 ($Ni^+ + H_2O$); black diamonds: R9 ($Ni^+ + CO_2$); grey circles: R8 ($Ni^+ + N_2$); grey triangles: R7 ($Ni^+ + O_2$). Note the two different ordinates: left hand ordinate for reactions R6 and R9; right hand ordinate for R7 and R8 (indicated with arrows). T = 294 K. The lines are linear regression fits through the experimental data, the slopes of which yield the 3rd order rate coefficients.

Figure 4. k' for reaction 1 plotted as a function of $[O_3]$, for 3 cases: a) $Ni^+ + O_3$ with full recycling of NiO^+ by reaction R2a (grey diamonds are measurements, dotted line is the model fit, extrapolated to $[O_3] = 0$ with the sparse dotted line); b) $Ni^+ + O_3$ with added $[H_2O] = 3 \times 10^{12}$ cm^{-3}, which reduced the recycling of NiO^+) (black triangles are measurements, black solid line is the model fit); and c) the limiting case of $Ni^+ + O_3$ with no recycling by R2a (black dashed line). The shaded regions correspond to the model fits ± 1σ. Conditions: 1.0 Torr, 294 K.

Figure 5. The fractional recovery in $[Ni^+]$ (where 0 is the Ni^+ concentration when [CO] = 0), as a function of $[CO]/[O_3]$. The solid points are experimental data, and the solid black line is the model fit with the ±1σ uncertainty shown by the shaded region. Conditions: 1 Torr, 294 K.

Figure 6. $[Ni^+]$ as a function of $[O_3]$, showing the increased recycling of Ni^+ in the presence of O. When $[O] = 9.2 \times 10^{12}$ molecule cm^{-3}, the experimental points (black triangles) and model fit (black line) should be compared with the experimental points (grey diamonds) and model fit (grey line) in the absence of O. The shades envelopes depict the ±1σ uncertainties of the model fits. Conditions: 1 Torr, 294 K, $[N_2] = 3.0 \times 10^{15}$ cm^{-3}.

Figure 7. Geometries of NiO^+, $Ni^+.H_2O$, $Ni^+.CO_2$, $Ni^+.N_2$, NiO_2^+, $NiO^+.CO_2$, $ONiO_2^+$, $NiO^+.H_2O$ and $NiO^+.N_2$ ions calculated at the B3LYP/aug-cc-pVQZ level of theory.[22]

Figure 8. Potential energy surface of quartet spin multiplicity for reaction 5, $NiO^+ + CO$, calculated at the B3LYP/aug-cc-pVQZ level of theory.

Figure 9. RRKM fits (thick lines) through the experimental data points (solid circles) for the recombination reactions of Ni^+ with N_2 (green), O_2 (blue), CO_2 (red) and H_2O (black). The faint lines indicate the sensitivity of each fit to α, the temperature-dependence of $\langle\Delta E\rangle_{down}$, varying between -0.5 and 0.5.

727 **Figure 10.** Removal rates of Ni^+ (panels (a) and (b)), and NiO^+ (panels (c) and (d)) in the
728 upper atmospheres of Earth (panels (a) and (c), 40^oN, local midnight, April) and Mars (panels
729 (b) and (d), local noon, latitude = 0^o, solar longitude $L_s = 85^o$).

730